THREE-DIMENSIONAL MESOSCALE MODEL FOR ANTHROPOGENIC AND CLOUD AEROSOL TRANSFER WITH ACCOUNT OF INTERACTION BETWEEN RADIATIVE AND MICROPHYSICAL PROCESSES AND OROGRAPHY. PART II. COMPUTATION RESULTS

K.Ya. Kondrat'yev, V.G. Bondarenko and V.I. Khvorost'yanov

Central Aerological Observatory, Dolgoprudnyi
Received August 3, 1988

The three-dimensional mesoscale model formulated in Part I was used in numerical experiments to study optical, microphysical, and aerosol relations, cloud and fog formation in an orographycally inhomogeneous atmospheric boundary layer (ABL), and the spread of aerosol interacting with condensate fields. The model is being used to study the interconnections between aerosol emissions, optical and radiative characteristics of the atmosphere, and microphysical parameters of clouds and fogs. We have studied the effect of orography on the spread of pollutants from diverse sources, and also the peculiarities of the spread of the light and heavy species of aerosol emissions in ABL.

Three sets of numerical experiments have been carried out using the model described in Part I of this paper. In the first set (experiments 1 and 2) we studied the effect of orography on the cloud and fog mesostructure, optico-aerosol relations, and the spread of aerosols interacting with condensate fields. In the second set we studied the effect of various model surface inclination angles on the spread of aerosols from ground-based and elevated point sources (experiments 3 and 4), and also from a vertically extended source (experiments 5 and 6). In the third set we simulated the transfer of aerosols and their deposition on a flat underlying surface from an elevated point source (experiment 10) and a linear vertically extended source (experiments 7–9) (see Table 1).

TABLE 1.

№ exp	Model area $X \times Y$ km^2	ABL height H_p m	Orography (hill height) h m	Initial temperature / Humidity H %	Source coordinates x_s, y_s m	Source altitude z_{s1} / z_{s2}	Type of sources	R_e μm
1	15 x 15	600	(200)	272.15 / 85	6.0;6.0	(10)	point	25
2	- " -	- " -	- " -	272.15 / 90	- " -	- " -	- " -	40
3	- " -	- " -	- " -	273.15 / 70	4.5;4.5	- " -	- " -	25
4	- " -	- " -	- " -	- " -	- " -	(260)	- " -	25
5	400 x 400	1.200	(300)	293.15 / 70	120;120	0/360	linear	1
6	200 x 200	- " -	- " -	- " -	60;60	- " -	- " -	25
7	400 x 400	- " -	absent	- " -	100;40	- " -	- " -	1
8	200 x 200	- " -	- " -	- " -	- " -	- " -	- " -	25
9	- " -	- " -	- " -	- " -	- " -	- " -	- " -	40
10	- " -	- " -	- " -	- " -	- " -	(400)	point	25

In experiment 1, the initial surface temperature T_{x1} = 272.15 K the altitude temperature distribution by height: $T(z) = T_{x1} - \gamma z$, the initial temperature for the hill surface was taken as $T_0(x, y) = T_{x1} - \gamma_a \delta(x, y)$, i.e., in the course of its forced uplift up the slope the air cools according to the dry adiabatic law. The profile q was given as $q(z) = \left(\frac{H-100}{100}\exp\left(-\frac{z}{A_D}\right)\right)$. The time $t = 0$ is 8:00 p.m., H = 85%, A_D = 550 m, H_p = 600 m. The height of the model hill h = 200 m.

As a result of the nocturnal long-wave cooling ($R_0 \sim -60 \div -70$ W/m^2), a temperature inversion occurs in the air layers close to the surface, with its upper boundary rising to a height of 200–250 m due to turbulence. The detailed vertical resolution of the model makes it possible to study at length the structure of a stable stratified flow deformed by an orographic inhomogeneity. We examined flows with small Froude numbers when the flow mostly passes around the obstable ($F_r = \frac{u}{NH_p}$, where $N = \sqrt{\frac{g_a(\gamma_a - \gamma)}{T_0}} \sim \sim 10^{-2}$ s^{-1} is the Brent-Vyaisyal frequency, whence $F_r \sim 0.5 \div 2$). The wavelength "generated" by the flow around the obstacle $\lambda = \frac{2N}{(N/u)} \sim 2 \div 3$ km. Numerical computations show that in the lower part of ABL on the windward slopes of the hill there are two upcurrent maxia resulting from the side flow around the hill (Fig. 1a).

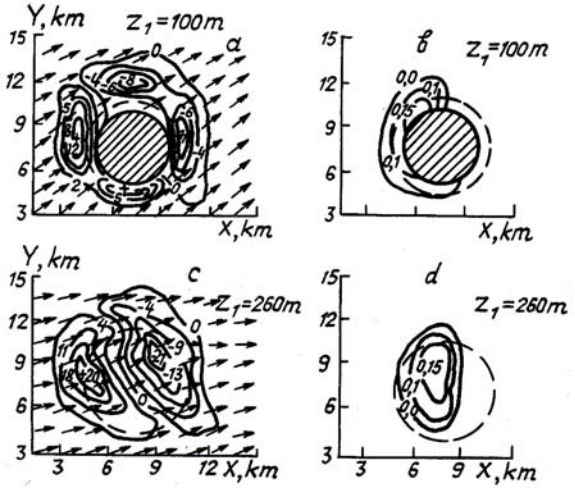

FIG. 1 Cross-sections of vertical motion fields w,cm/sec (curves a and b) and fog water content q_L, g/kg (curves b and d) over the hill in horizontal planes xoy at the heights z_1 = 100 m (curves a and b) and z_1 = 260 m (curves c and d) in experiment 1 (the shaded area is the section of the hill, the dashed line is its foot, and the arrows represent the horizontal velocity vectors C at the grid nodes).

These give way to downcurrent at the leeward slopes that also exhibit two maxima resulting from the spreading of the frontal portion of the flow. As the altitude grows higher, the effect of the side flow declines and the areas of upward and downward motions merge. Moreover, due to the observed right-hand turn of the wind with altitude in ABL, they are reoriented towards the background wind direction (Fig. 1c).

The patterns of the stably stratified flow past bell-shaped obstacles as computed with the model agree with physical experiments[1] and simulations[2,3], except that the experiments did not reproduce the altitude wind "rotation" observed in ABL and, consequently, no spatial reorientation of the areas of upward and compensating downward currents was found.

In the flow around obstacles, fog is formed at the windward slope in the upcurrent areas (Figs. 1b, d). With a rise up the slope of the obstacle, the air is cooled according to the dry adiabatic law, since the incoming flow stratification is moisture-unstable, because of the $T(z)$ lapse rate mismatch, there occur disturbances over and beyond the obstacle that cannot be described by the quasipotential flow theory. Their character resembles internal gravitational waves (IGW). The wind velocity field deformation leads to a secondary maximum of ascending currents beyond the obstacle (Fig. 2a).

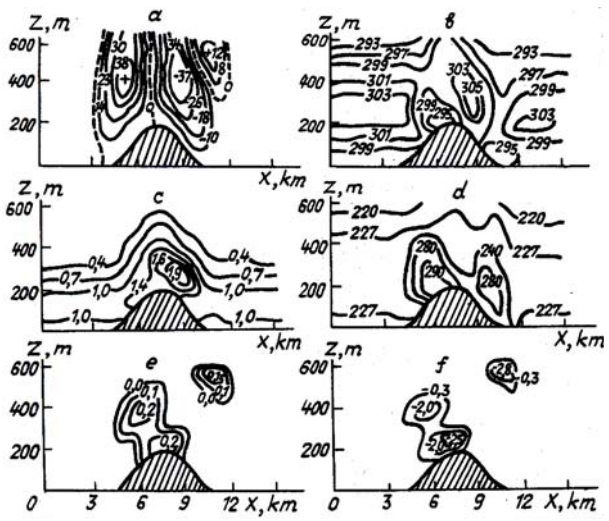

FIG. 2. Sections of vertical motion fields w, cm/sec (a); vertical turbulence coefficient k_z, cm^2/sec (c); long-wave radiation flows upward flux $F_1^{\uparrow}$ (b) and downward flux $F_1^{\downarrow}$ (c), W/m^2, cloud and fog water content q_1,g/kg (e) and radiation heat influx R_L, K/hr (f) over the hill (shaded area) in plane xOz at y = 7.5 km (experiment 1.)

As the flow passes over the hill it is turbulized, with ^increasing by 50–100 per cent (Fig. 2c). Such peculiarities of the flow structure lead to the formation of a fog on the windward side of the obstacle and of elevated clouds beyond it in the upcurrent areas (Fig. 2e). Being close to the blackbody radiation

fluxes $B(T)$, the upward radiation flows $F_1^{\uparrow}$ largely follow the structure of the temperature field (Fig. 2b). The presence of clouds and fog causes a sharp increase of the downward LWR ($F_1^{\uparrow}$ goes up to 280–290 W/m^2) in areas with a maximum water content gradient (Fig. 2d), i. e., the cloud acts to screen LWR, with a resultant change in the radiation balance of the underlying surface. Long-wave cooling shifts from the earth surface to the fog and cloud tops (where water content gradients are at a maximum) and amounts to –2, –2.8 K/hr (Fig. 2f). This deepens the temperature inversions at the top levels, contributes to the increase of q_L up to 0.2 g/kg owing to the positive feedback between R_L and q_L, which results in the increased heights of the cloud and fog tops (Figs. 2e and f). This is how one of the types of thecloud-radiation interactive coupling described above is realised. Thus, in the absence of advection, orography causes the formation of a double-layer cloud-fog system that develops under the influence of the radiation factor.

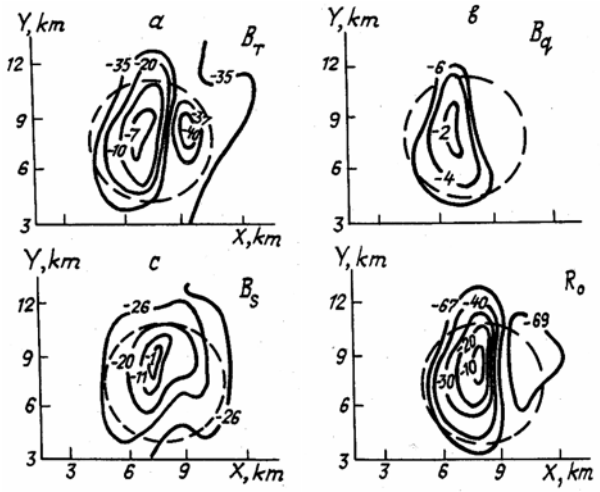

FIG. 3. Surface heat balance components (W/m^2): turbulent flows of sensible B (a) and latent B (b) heat, heat flow from the depth of the soil B_S (c) and radiation balance R_0 (d).

Figure 3 shows the surface heat balance component distribution(Eq. (17)). Nocturnal radiation cooling results in compensating turbulent flows towards the surface from the atmosphere: sensible heat $B_T = -c_p \rho k_z \left(\frac{\partial T}{\partial z} + \gamma_a \right)$ and latent heat $B_q = -c_p L k_z \frac{\partial q}{\partial z}$, and a heat flow from the soil $B_s = -c_s \rho_s \kappa_s \frac{\partial T_s}{\partial x}$. The fog and cloud formation alters the surface radiation balance. The near-surface temperature Inversion on the windward side of the obstacle is destroyed due to the following two factors: forced upcurrents and a wind velocity increase with height. The terms with $u\gamma_a\delta_x$, $v\gamma_a\delta_y$ in Eq. (7) account for additional cooling that shifts from the underlying surface to the fog top thereby stabilizing the vertical profile $T(z)$. This causes reduction of the near-surface inversion and turbulent heat B_T from the atmosphere to the surface (from –35 to –7 W/m^2) on the windward slope of the hill on the lee side of the hill, the air heated by the downcurrents increases the temperature lapse rate in the surface layer and deepens the inversion, B rises up to –40 W/m^2, for x = 8–9 km (Fig. 3a). The humidity inversion in the fog is destroyed as the condensate settles onto the underlying surface, B_q on the hill is one-third as much over the ambient latent heat (Fig. 3b). In view of the greenhouse effect of the fog, R_0 goes down from –70 W/m^2 to –18 W/m^2 (Fig. 3d). The local warming-up below the fog layer leads to a sharp drop in the compensating heat flow B_s from the depth of the soil to the surface from –30 to –10 W/m^2 (Fig. 3c). Thus, the combined effect of the radiative and orographic factors causes the spatial inhomogeneity of the surface heat balance components.

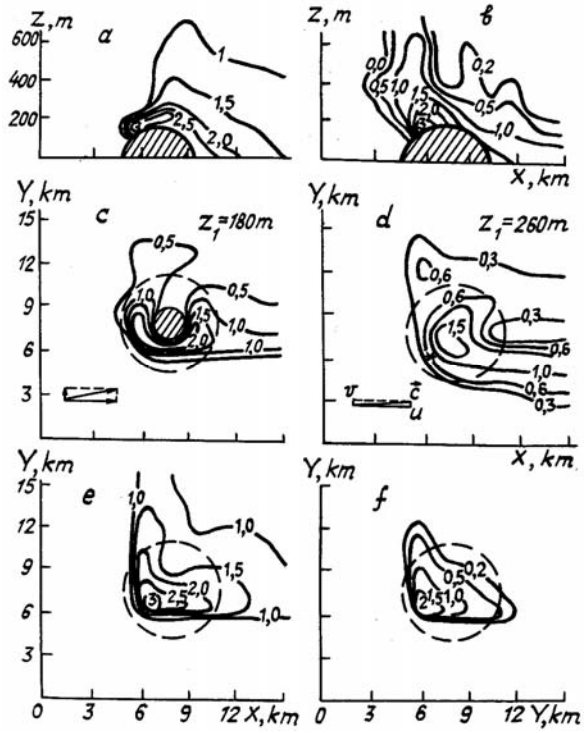

FIG. 4. Vertical sections of pollutant concentration fields lgS in planes xOz at y = 7,5 km (a) and yOz at x = 7.5 km (b); horizontal sections of fields IgS and velocity vector components C over the hill (h = 200 m) at heights of z_1 = 180 m (c) and z = 260 m (d); pollutant concentration near the ground (lgSe) and accumulated concentration on the underlying surface (F_s, f) in experiment 1 (the shaded area is a section of the hill, and the dashed line is its foot).

Spreading from a continuous point source placed at a height of z_s = 10 m at a point with coordinates

(6.6 km) on the windward slope of the obstacle (the initial concentration $S_{10} = 1 \times 10^4$ l^{-1}) the aerosol heavily absorbed by fog droplets on the windward side of the hill. A vertical section at right angles to the background wind and a horizontal section at $z_1 = 180$ m clearly shows maximum concentrations of lg S at the slopes of the hill (Figs. 4b, c). The maximum on its south-east side is due to the prevailing direction of the side flow around the obstacle (vector C), with the pollution accumulating on the condensate droplets. The aerosol particle absorption and the settling of the pollutant species entrained by fog droplets on the underlying surface result in the formation of a pollution patch .with maximum values of lgS_0 and accumulated sediment F_s on the windward slope of the obstacle (see Fig. 4d). A patch with minimum pollution is formed in the lee of the hill, which is due to the "screening" effect of the fog cap and the prevailing side flow of the aerosol cloud around the obstacle.

The results obtained agree with experimental data[4,5] and theoretical predictions[4,6] that show an increased aerosol number density in clouds and fogs (the pollution accumulation by the condensate).

The vertical optical thickness of the atmosphere is calculated from the formula[7,8]:

$$\tau_\lambda = \int_0^z (\sigma_{w\lambda}(z) + \sigma_{a\lambda}(z))\, dz \qquad (1)$$

where $\sigma_{w\lambda}$ and $\sigma_{a\lambda}$ are cross-sections of radiation scattering by droplets and aerosol, respectively. Calculations according to formulas for $\sigma_{w\lambda}$[9,10] show that in a fog up to 200 m thick with average water contents $q_L \sim 0.1$–0.2 g/kg and $\bar{r}_L = 5$ μm, $\tau_{w\lambda} \simeq 4$–10 at $\lambda = 0.5$ μm. The accumulated aerosol increases the optical thickness owing to the following factors:

1. The dependence of aerosol scattering cross-sections on wavelength λ and relative humidity H, according to experimental data is determined by empirical inverse-power laws $\sigma\lambda \sim \lambda^{-Q}$ (see Refs. 11 and 12) and $\sigma(H) \sim (1 - H)^{-R}$ (see Refs. 13–15) that can be derived theoretically from a model hygroscopic water-covered aerosol[16]:

$$\sigma_{a\lambda}(H) = D_1(\nu, \alpha)\, S\, \lambda^{-Q}\, (1 - H)^{-R} \qquad (2)$$

$$\sigma_{a\lambda} \mid_{H = 100\%} = D_3\, \lambda^{-P} \qquad (3)$$

where $D_1(\nu, \alpha)$ is a constant depending on the aerosol microstructure and S is the aerosol concentration. With an increase in relative humidity, $\sigma_{\alpha\lambda}(H)$ increases by several fold according to Eq. (1), and in a fog with $H = 100\%$, according to Eq. (3), $\sigma_{\alpha\lambda} = 1$–$3$ km^{-1}. In polluted areas aerosol optical thickness estimated by the given model may amount to 1–3.

2. The aerosol modifies the cloud and fog microstructure, leading to a reduced droplet size. According to Refs. 10 and $\sigma_{w\lambda}(r_L) \sim r_L^{-1}$. In the areas of heavy pollution (Fig. 4, $x = 7$ km, $y = 6$ km), owing to activation of new condensation nuclei from aerosol particles, the mean droplet size is reduced by 30–50%. According to $\sigma_{w\lambda}(r_L)$, there is a corresponding increase in the scattering cross-section and optical thickness (up to 12–15).

Thus, anthropogenic aerosol emissions in the presence of clouds and fogs can be detected through remote sensing of the atmosphere as zones with increasing radiation scattering cross-sections and optical thickness. This agrees with experimental data[5,9].

In the second set of experiments, we studied the spread of aerosol particles in the absence of clouds or fog ("dry problem") over an orographically inhomogeneous underlying surface with variable inclination angles (Table 1). Thus, with a hill height $h = 200$ m and a test area of 15×15 km^2 (experiment 3), separation of the incoming stratified flow determines the existence up to considerable heights of a spatial pollution field inhomogeneity spreading from an elevated source ($z_s = 20$ m).

The distribution of the above ground concentration S_0 and accumulated sedimentary pollutants F_s indicates the existence on the lee side of the hill of a lower precipitation zone ("precipitation shadow") formed due to moderation of the direct incoming flow by an orographic obstacle and an intense side flow of the aerosol cloud around the hill.

A comparison of the computational data with the measurements of the pollution spread over the surface of a bell-shaped obstacle in a physical model experiment[18] shows them to be in reasonable accord with each other: the accumulated impurity concentration is at a maximum' on the windward slope and at a minimum on the leeward slope and the isoline pattern lgS shows that the flow and the pollution cloud mostly pass around the flanks of the obstacle (numerical calculations for real topography[19] show the same effect).

Given an elevated point source located at a considerable height ($z_{s1} = 240$ m, experiment 4), the pollution cloud is carried more intensively in the sideways direction from the hill by the deformed air flow. The contamination plume gets wider transverse to the background wind at heights with a maximum transverse component v of the horizontal wind velocity C.

Experiments 5 and 6 involved more gently sloping obstacles with maximum heights of $h = 300$ m. For given horizontal scales ($x \sim 200$–400 m), the surface slopes are small ($\sim 10^{-3}$). At low wind velocities ($U_a = G = 5$m/sec) a quasipotential flow around the obstacle is observed without any significant deformation of the incoming air flow. The altitude of pollution plumes follows the changes in the terrain profile, and it is only in areas with slight upcurrents over the windward slopes of the obstacles where the aerosol particles tend to rise higher. Thus, the experiments with a negligible orographic inhomogeneity of the underlying surface ($\tau\gamma\alpha_\sigma \leq 0.001$) confirm the conclusion formulated in Ref. 4 that a gently sloping relief has no appreciable effect on the pollution transfer.

A nonuniform spatial distribution of sedimenting pollutants and accumulated sediments on the surface does occur only at increased slopes ($tg\alpha_s \sim 0.05$–0.1, experiments 3 and 4).

In experiments 5–9, a vertically extended linear source was used to simulate ejections into the atmosphere of initially overheated pollutants from industrial sources, thermal power plants, combustion products, etc. Estimates in Ref. 4 show that with the initial overheating $\Delta T \sim 50$ K the height of the initial aerosol plume uplift increases up to 600 m. Given linear sources at the nodes of the difference grid (Δx_s, Δy_s) the spread of emissions from area sources whose linear extent did not exceed the step of the difference grid (1.5–2 km) was simulated. The spread of aerosol components with different weights was studied: from virtually weightless species ($R_e = 1$ μm, simulating the transfer of condensation and crystallization nuclei) to particles with $R_e = 25.40$ μm (coarse dust fractions, combustion products) (Table 1).

In the computations the linear source was set at the grid nodes in the vertical at the altitudes $z_{s1} = 0$ m, $z_{s2} = 360$ m, with a northern background wind $U_a = G = 5$ m/sec. The surface temperature $T_{x1} = 273.15$ K. The choice of the spatial scale in the model (400×400 km^2, 200×200 km^2) was dictated by the need to evaluate the spreadzones for aerosol components of variable size. In experiment 7, the aerosol particle size $R_e = 1$ μm, the initial concentration $S_{10} = 2 \times 10^4$ l^{-1}, and the vertically extended linear source coordinates $x_s = 100$ km, $y_s = 40$ km (Table 1). The tail cone of a virtually weightless pollutant with $R_e = 1$ μm rises to heights of $z \sim 600$ m (Fig. 5a, b).

As a result of nocturnal long-wave cooling, the surface temperature inversion extends to a height of ~ 200 m beyond which there are layers with a neutral stratification (Fig. 5b). In view of a virtual absence of aerosol sedimentation the pollution spreads in a horizontal direction above the surface temperature inversion layer (at heights of 300–600 m) far away from the source(Fig. 5a and b). The temperature rise up to a height of ~ 200 m determines low ABL turbulization (profile k_z, Fig. 5a) and altitude changes in the ground wind deflection angle α_s from the background wind (Fig. 5b). The light-weight aerosol plume broadening in the transverse direction with respect to the average wind is peaked at heights of 200–500 m, where the transverse horizontal wind velocity component is at a maximum (Fig. 5b). The results obtained agree with the evaluations of the spread of considerably overheated contaminants at night and in the evening when the surface temperature inversions are often found to occur. In these conditions the pollution may not reach the ground and will disperse above the inversion layer.

In view of such peculiarities inherent in the wind transfer of a light-weight aerosol it is carried far away from the source and settles on the underlying surface under the influence of the turbulent diffusion to form a patch of pollution extended in the direction of the average wind. As a result of a 10-hour aerosol emission into the atmosphere, a minute quantity of sediment is accumulated on the earth's surface, while the bulk of the matter is diffused from the elevated plumes; the accumulated sediment concentration decreases by an order of magnitude every 50–70 km downstream (Fig. 5d).

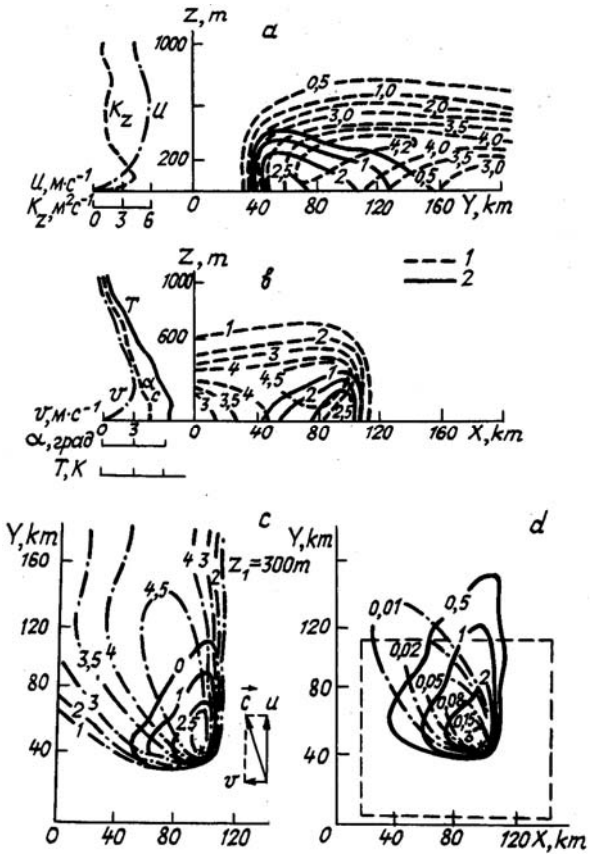

FIG. 5. Vertical sections of pollution concentration fields (lgS) along and across the background wind (in plane y0z at x = 80 km. a, and in the plane x0z at y = 100 km. b). vertical profiles of meteorological elements: longitudinal component of horizontal wind velocity u, m/s, vertical turbulent diffusion coefficient k_z, m /sec (a), temperature T K, transverse wind velocity component v, m/s, deflection angle of horizontal wind from background wind α_C, degrees (b), and horizontal sections of pollution concentration fields lgS : at a height of $z_1 = 300$ m, horizontal velocity vector components C (c), and accumulated pollution concentration F_S (d) in experiments 7, 8 after a 10-hour evolution of the pollution plume facula (1-light pollutant component $R_e = 1$ mm; 2-heavy component, $R_Э = 25$mm).

Aerological measurements on the spread of condensation nuclei (CN) point to areas of increased CN-concentration due to certain industrial sources. Thus, experiments carried out in 1971–1975 under the

METROMEX project showed that at a height of 600 m above sea level downwind from Saint Louis the CN concentration was greater by an order of magnitude than that observed upwind of the area, with the horizontal extent of the enhanced CN concentration zones ranging from 30 to 50 km[20]. Large quantities of CN led to changes in the cloud microstructure (the mean droplet diameter downwind from the industrial zone was 2–3 μm smaller, and the water content was 10–15% higher than upwind).

In experiments 8 and 9, the spread of heavier aerosol components with mean sizes R_e = 25 μm and R_e = 40 μm over an area of 200×200 km^2 (Table 1) was studied.

Owing to a more intense gravitational settling of heavy aerosol particles, the plume top does not exceed the initial height of the source (360 m). Within 8 hours from the start of the counting a dynamic equilibrium is established between the ejection of aerosol particles into the atmosphere and their settlement on the underlying surface. The sedimenting pollutant is carried along descending paths from the emission line to the earth surface (Figs. 5a and b) in contrast to the weightless component that spreads above the barrier inversion layer. Since the wind in ABL makes a 25–35° right-hand turn with height the settling aerosol tends to exhibit a fan-shaped spread pattern (Figs. 5c and d). The surface pollution dramatically increases as the size of the settling particles grows larger. In 10 hours the accumulated sediment on the earth's surface in experiment 8 takes the form of a fan-shaped patch, and F_s is on the average reduced by an order of magnitude every 30–50 km downstream (Fig. 5d). The calculations in experiment 9 with particle size R_e = 40 μm show that due to a more intense settlement of the pollutant onto the underlying surface the sediment is localized near the source, forming a patch with a finite length and width. The accumulated concentration decreases by an order of magnitude every 20–30 km in the direction of the average wind.

The sediment trail distribution from an elevated point source in experiment 10 differs from that of the fan-shaped patches in experiments 7–9 by a smaller variance of the settled particles along the x axis and a greater extension towards the direction of the background wind (y axis).

The analysis of the results obtained from the numerical simulations allow us to draw the following conclusions. The proposed model provides an adequate description of the cloud-radiation and optico-aerosol relations on a mesometeorological scale in an orographically inhomogeneous ABL and permits the effects of anthropogenic environmental pollution to be assessed. We have evaluated the influence of orographically inhomogeneous surfaces on the fog and cloud formation, analyzed their role in the change of radiation conditions across the whole ABL width, and studied the distribution patterns for aerosol particles with different weights under different types of stable temperature stratification determined by the cloud-radiation interconnections. Thus, our computations show that over anthropogenic pollution areas with an orographically inhomogeneous underlying surface (as in cities) the cloud and aerosol distribution may differ considerably from statistical average optico-aerosol and cloud-radiation models of the atmosphere, which is confirmed by observational data[5,9,21].

These computations may facilitate the design and realization of experiments in the optical monitoring of polluting emissions and remote sensing of the atmosphere over industrial areas, in particular, in studying the effect of urban activities on the optical characteristics of the atmosphere and microclimate.

REFERENCES

1. J.C.R. Hunt and W.H. Snyder J. Fluid Mech., **96**, 671 (1980)
2. P.W.H. Quart. J. Roy. Met. Soc., **104**, 289 (1978)
3. Orographic effects in planetary flows. CARP, 452 (1980)
4. M.Y. Berlyand *Current Problems of Atmospheric Diffusion and Pollution of the Atmosphere* (Gidrometeoizdat, Leningrad, 1975)
5. B.D. Belan, G.O. Zadde and T.M. Rasskazchikova Meteorolog. Gidrolog., 38 (1987)
6. I.P. Mazin Meteorolog. Gidrolog., 3 (1982)
7. K.Ya. Kondrat'yev, N.I. Moskalenko and D.V. Pozdnyakov *Atmospheric Aerosol* (Gidrometeoizdat, Leningrad, 1975)
8. V.E. Zuev and G.M. Krekov *Optical model atmospheres Modern Problems of Atmospheric Optics* (Gidrometeoizdat, Leningrad, 1986)
9. K.Ya. Kondrat'yev and B.I. Binenko *The Effect of Clouds on Radiation and Climate* (Gidrometeoizdat, Leningrad, 1984)
10. K.Ya. Kondrat'yev, M.V. Ovchinnikov and V.I. Khvorost'yanov Optika Atmosfery, **1** (1988)
11. H. Junge *Chemical Composition and Radioactivity of the Atmosphere Russian translation* (Mir, Moscow, 1965)
12. K.Ya. Kondrat'yev Actinometry (Gidrometeoizdat, Leningrad, 1965)
13. F. Kasten Tellus, **21**, (1969)
14. G. Hanel Beitr. Phys. Atmos., No. 2 (1971)
15. M.V. Panchenko Optika Atmosfery, **1**, 25 (1988)
16. V.I. Khvorost'yanov Meteorolog. Gidrolog., 28 (1980)
17. G.I. Marchuk, K.Ya. Kondrat'yev, V.V. Kozoderov et al. *Clouds and Climate* (Gidrometeoizdat, Leningrad, 1986)
18. W.H. Snyder and R.E. Britter Atm. Environ., **21**, 735 (1987)
19. G. Gross, H. Vogel and F. Wipperman Atm. Environ., **21**, 483 (1987)
20. G.Y. Lansberg *Urban Climate* (Gidrometeoizdat, Leningrad, 1983)
21. K.Ya. Kondrat'yev and V.I. Binenko Boundary Layer Meteorol., **41**, (1987)